PAPER

Check for updates

Novel mesoporous bismuth oxyiodide single-crystal nanosheets with enhanced catalytic activity

Hang Liu, [ID] †[a] Jian Cai,†[b] Man Luo,[a] Chang Chen*[c] and Pei Hu*[a]

A simple one-step approach was employed to fabricate novel BiOI nanosheets and mesoporous $Bi_4O_5I_2$ single-crystal nanosheets. The formation mechanism of the as-prepared two-dimensional mesoporous sheet-like structure and photocatalytic activities were systematically discussed. The stripping effect of I_2 vapor generated in the calcination process was concluded to be responsible for the formation of this two-dimensional mesoporous structure. Moreover, relying on this advantage, $Bi_4O_5I_2$ displayed excellent activities in the degradation of RhB and salicylic acid under visible light irradiation.

1. Introduction

In recent years, the rise of graphene and graphene-like materials has aroused tremendous interests in two-dimensional (2D) structures due to their fascinating mechanical, thermal, optical, and electrical properties including high electrical conductivity and flexibility and high specific surface areas.[1–5] A variety of 2D sheet-like and layered materials, for instance, MoS_2, SnS_2, C_3N_4, Bi_2O_3, TiO_2, *etc.* or materials assembled by 2D structural units such as nano/micro-flowers, hollow spheres, *etc.* have been widely reported in succession.[6–12] These materials have pushed the research on solar power, signal conversion, clean energy, and environmental remediation.[13–15] However, low-cost and efficient photonic devices, photovoltaic conversion systems, sensors and catalysts require not only highly accessible surfaces, but also long-range electronic connectivity and continuous structures.[16,17] 2D mesoporous single-crystal nanosheets can meet these criteria perfectly.[18–20] Unlike traditional 2D structures, which suffer from the lower utilization of inside bulk materials, 2D mesoporous single-crystal nanosheets can supply more active sites and better contact with the inside bulk materials.[21–24] However, the pore structures of the existing mesoporous materials are mainly 3D, which makes it difficult to introduce active ingredients into the 3D pore canals and leads to a poor availability of the inside bulk material.[25–27] Besides, all previous approaches for synthesizing mesoporous materials have used sacrificial templates, the processes of which are

complicated.[28–30] To solve these problems effectively, developing a template-free method to fabricate 2D mesoporous single-crystal nanosheets is meaningful. However, only few studies focus on such materials and rarely involve mechanism studies.

Generally, 2D materials are synthesised by means of the chemical and mechanical exfoliation of layered compounds, hydrothermal method and chemical vapor deposition. However, these methods are all complicated and it is difficult to obtain mesoporous structures.[31]

Bismuth oxyhalides (BOX, X = Cl, Br and I) are known for their unique layered structures, high activity and high photo-corrosion stability features and are recognized as promising photocatalyst candidates.[32] Thereinto, bismuth oxyiodide (BOI) has the widest visible light absorption region and excellent photocatalytic efficiency and thus has drawn great attention in many areas. In general, except BiOI, the BOI series also includes I-poor materials, in which more I atoms are substituted by O atoms, such as $Bi_4O_5I_2$, $Bi_7O_9I_3$, α-Bi_5O_7I and β-Bi_5O_7I.[33,34] Among these BOI materials, most attention has been paid to the 3D structured BiOI, Bi_5O_7I and $Bi_4O_5I_2$, which can be easily prepared, but only few studies have focused on 2D materials. Lee *et al.* synthesized a range of BOI materials with diverse morphologies by the hydrothermal method, but the existence of so many reactants makes it hard to get pure BiOI and Bi_5O_7I.[35] Yin *et al.*, Hou *et al.* and Xiao *et al.* have reported nano-structured $Bi_4O_5I_2$ successively including nano-flakes and nano-roses fabricated *via* a complicated organic solvent method.[36–38]

To the best of our knowledge, there has been no report on the synthesis and application of porous $Bi_4O_5I_2$ nanosheets. Herein, we prepared novel mesoporous $Bi_4O_5I_2$ single-crystal nanosheets using a simple one-step method. By systematic research, we demonstrated the formation mechanism of these mesoporous $Bi_4O_5I_2$ nanosheets. Moreover, the application research showed that the as-prepared mesoporous $Bi_4O_5I_2$ nanosheets possessed enhanced visible light photocatalysis

[a]State Key Laboratory of Materials Processing and Die & Mould Technology, School of Materials Science and Engineering, Huazhong University of Science and Technology, Wuhan 430074, P. R. China. E-mail: hupeisysdoing@hust.edu.cn; Tel: +86 27 87558241

[b]State Key Laboratory of Lake Science and Environment, Nanjing Institute of Geography and Limnology, Chinese Academy of Sciences, Nanjing 210008, P. R. China

[c]School of Resource and Environment Science, Wuhan University, Wuhan 430070, P. R. China. E-mail: bulenigt@foxmail.com

† Hang Liu and Jian Cai contributed equally.

activity and good stability towards the degradation of two pollutants.

2. Materials and methods

2.1 Synthesis of bismuth oxyiodide

All the chemical reagents were purchased from Aladdin and used as received. In a typical procedure, 0.5 g BiI$_3$ bulk was placed in a corundum boat and then annealed at 300 °C for 3 h under air atmosphere with a heating rate of 5 °C min^{-1}. After cooling, the treated BiI$_3$ was washed three times with ultrapure water and anhydrous ethanol and dried under vacuum at 80 °C. Finally, the pre-processed BiI$_3$ was further annealed at 350 °C, 400 °C and 450 °C (the corresponding samples were named as BOI-350, BOI-400 and BOI-450) for 3 h, and the heating rate was 3 °C min^{-1}.

2.2 Material characterization

The structure and morphology of the products were characterized by X-ray diffraction (XRD, PANalytical B. V., Holland) using Cu Kα$_1$ irradiation (λ = 1.5406 Å), scanning electron microscopy (SEM, FEI, Sirion 200), and transmission electron microscopy (TEM, JEOL JEM-2010F). Nitrogen adsorption/desorption measurements were recorded using a 77 Kon a Micromeritics ASPA 2020 analyzer. Thermogravimetric analysis (TGA) was performed in air and N$_2$ separately on Pyris 1 TGA (PerkinElmer Instruments) with a heating rate of 10 °C min^{-1}. UV-vis diffuse reflectance spectra (DRS) were recorded on a SHIMADZU UV-2550 spectrophotometer with an integrating sphere, and BaSO$_4$ was used as the reference.

2.3 Photocatalytic activity and durability tests

Photocatalytic activity tests were carried out in a self-made cylindrical glass vessel with a water-cooling jacket for the degradation of RhB (100 mL, 1 × 10^{-5} mol L^{-1}) and salicylic acid (100 mL, 20 mg L^{-1}) under visible light irradiation. The visible light was obtained by a 500 W Xe lamp at ambient temperature. A 420 nm long-pass glass filter was used to sacrifice the wavelength of the incident light in the reactions. The irradiation distance between the lamp and the sample was 12 cm. In a typical procedure, the RhB solution or salicylic acid solution containing 0.100 g of the BOI sample was put in a homemade reactor. The suspension was stirred for 12 h in dark to reach an adsorption–desorption equilibrium between the organics and the catalysts and then exposed to a 500 W Xe lamp. At a given time interval, 3 mL of the reaction solution was taken out of the suspension and immediately centrifuged at 12 000 rpm for 4 min. The supernatant was analyzed by UV/vis spectroscopy (Shimadzu UV2550). The reaction was performed under constant magnetic stirring under ambient conditions.

In order to evaluate the durability of BOI, five cycles of photocatalytic measurements were employed under the same conditions of the above-mentioned photocatalytic activity test. The photocatalyst was separated from the aqueous solution and washed by ultrapure water and anhydrous ethanol after each reaction cycle.

3. Result and discussion

3.1 XRD analysis

Fig. 1 shows the XRD patterns of the as-prepared bismuth oxyiodide (BOI) samples. As shown in Fig. 1a, every XRD pattern has a similar peak curve; all the observed peaks of BOI-350 can be indexed to tetragonal BiOI (JCPDS no. 10-0445 and ICSD-391354) and no other residual phase, such as BiI$_3$, is detected. This indicates that BOI-350 is pure BiOI.[38] Similarly, according to the major diffraction peaks at 28.68°, 31.29°, 37.11°, 45.04°, 49.20°, and 54.22°, the XRD pattern of BOI-450 can be indexed to monoclinic Bi$_4$O$_5$I$_2$ (ICSD-412590). For BOI-400, there is no single crystal structure matching its diffraction peaks well except orthorhombic Bi$_3$O$_4$Br (JCPDS no. 84-0793). Since no reactant that contains Br was used in the synthesis process, BOI-400 could be only attributed to the mixed phase of BiOI and Bi$_4$O$_5$I$_2$.[39] For the sake of comparing and analyzing the difference in the crystal structures of the three BOI samples further, partial enlargement XRD patterns were acquired (Fig. 1b). It is noticed that (marked with an arrow) the main double peaks located between 25° and 35° shift to smaller angles with the gradual increase in the calcination temperature. Besides, along with the angle deviation, the weak peak at 9.5° disappears as well, as denoted in the dotted box. All the phenomena mentioned above indicate that the heat-treatment process plays an important role in the conversion and formation of new crystal structures.

3.2 TG analysis

To further demonstrate this conclusion and explore the reaction mechanism, TGA was carried out to determine the phase transformation details of the BOI samples in the annealing process. Fig. 2a displays the TGA curve of bulk BiI$_3$ in an air flow. It is found that there is no obvious change in BiI$_3$ for temperatures below 300 °C. However, when the temperature reaches 350 °C, a dramatic weight loss is observed. From 350 °C to 480 °C, the total weight loss of bulk BiI$_3$ is up to 92%, which means that the bulk BiI$_3$ is completely changed when calcination is continued. With the further increase in the temperature, the weight loss of BiI$_3$ is sustained but only 5%. At the end of the heating process, no more weight loss appears, and the reaction residue becomes stable.
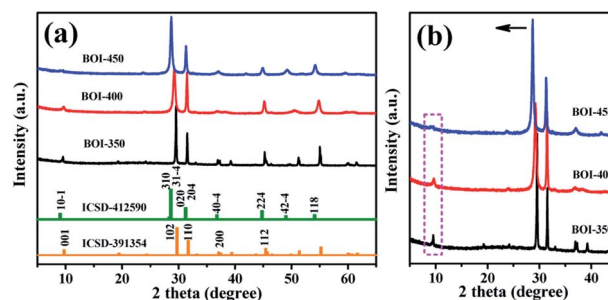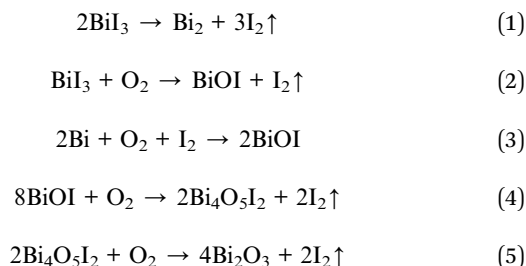

Fig. 1 XRD patterns of BOI samples (a) and their partial enlargement (b).

Fig. 2b shows the TGA curve of bulk BiI_3 in an N_2 flow. As shown in Fig. 2b, the first 11% weight loss occurs between room temperature and 265 °C, and this can be attributed to the dehydration of BiI_3. As the temperature rises, almost no weight loss occurs from 265 °C to 550 °C, which means that the bulk BiI_3 is very stable in this temperature range. However, with the heat treatment proceeding, a significant weight loss occurs after 550 °C and continues until the process ends. This calcination behaviour of BiI_3 is distinct from its previous performance in an air flow, indicating that oxygen is critical to the formation of the as-prepared BOI samples. The total weight loss of the above-mentioned stages is about 52%. Considering that the melting point and boiling point of BiI_3 are 408.6 °C and 542 °C, respectively, the weight loss behaviour of BiI_3 in an N_2 flow is in good agreement with the following reaction eqn (1):

$$2BiI_3 \rightarrow Bi_2 + 3I_2\uparrow \tag{1}$$

$$BiI_3 + O_2 \rightarrow BiOI + I_2\uparrow \tag{2}$$

$$2Bi + O_2 + I_2 \rightarrow 2BiOI \tag{3}$$

$$8BiOI + O_2 \rightarrow 2Bi_4O_5I_2 + 2I_2\uparrow \tag{4}$$

$$2Bi_4O_5I_2 + O_2 \rightarrow 4Bi_2O_3 + 2I_2\uparrow \tag{5}$$

Because of the lower melting point, I_2 will first evaporate completely and when this is finished, the total weight loss of reaction (1) is about 55%, which matches well with the data in Fig. 2b.
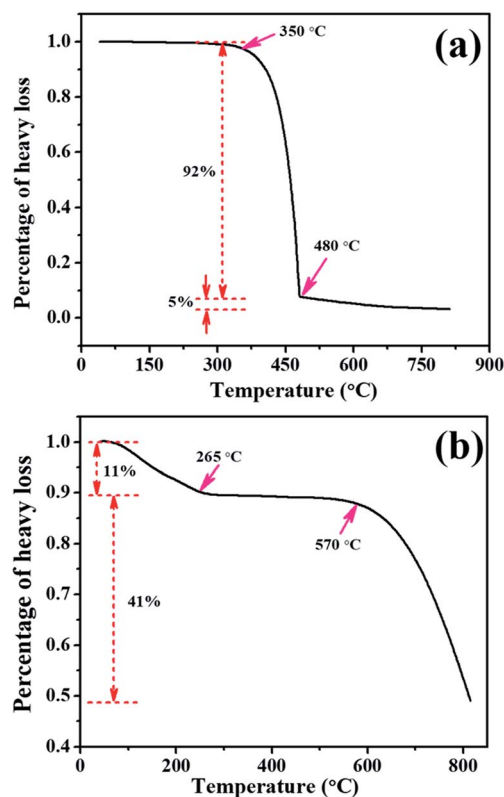
According to the analyzed results of the XRD patterns and TGA curves, the formation process of the as-prepared BOI samples can be concluded as per the above-mentioned reaction eqn (2)–(5).

In reaction (2), BiI_3 reacts with oxygen first and generates rust-red BiOI and iodine vapor. In reaction (3), Bi generated from the BiI_3 decomposition continues to react with oxygen and iodine vapor to form BiOI. As the reaction proceeds, the formed BiOI is oxidized by oxygen steadily and produces yellow $Bi_4O_5I_2$ and iodine vapor, as shown by reaction (4). In reaction (5), the prepared $Bi_4O_5I_2$ reacts with oxygen further and finally generates stable Bi_2O_3 and iodine vapor. Then, the residual mass of the whole system changes slightly.

3.3 SEM and TEM analyses

The morphology and microstructure of the as-prepared BOI samples were further investigated by SEM and TEM. Fig. 3 shows the SEM images of the BOI samples. It can be seen that all the three samples consist of individual but mutually over-lapping nanosheets, and some of these nanosheets possess perfect right angles. Fig. 3d shows the theoretical crystal structures of the as-prepared BOI samples. According to the XRD patterns mentioned above, during the calcination of bulk BiI_3, the first generated sample was BiOI with a tetragonal crystal structure and under certain conditions, tetragonal BiOI preferred to form a two-dimensional (2D) sheet-like structure. Because the subsequent reactions were just the oxidation of BiOI and the release of iodine vapor on the macro scale, the 2D sheet-like structure of BiOI survived on the micro scale and all the BOI samples retained this sheet-like structure. Thus, in this regard, the XRD and SEM results match each other well.

Fig. 4 shows the typical TEM images and selected area electron diffraction (SAED) patterns of the BOI samples. As shown in Fig. 4, all three BOI samples are composed of nanosheets with right angles. This situation is in accordance with the SEM
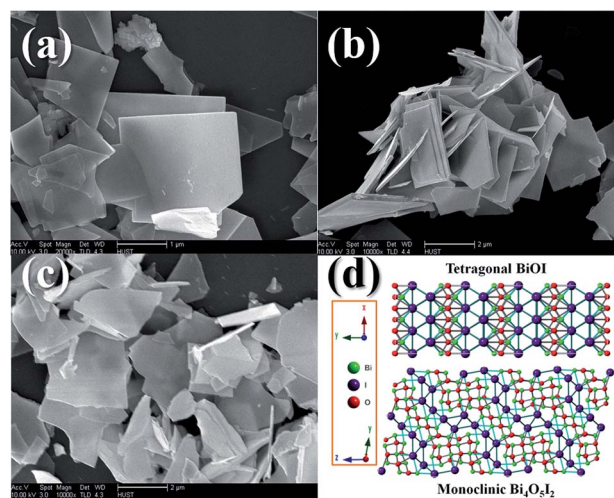

Fig. 3 SEM images and theoretical crystal structures of the BOI samples: (a) BOI-350; (b) BOI-400; (c) BOI-450; (d) crystal structures of BiOI and $Bi_4O_5I_2$.

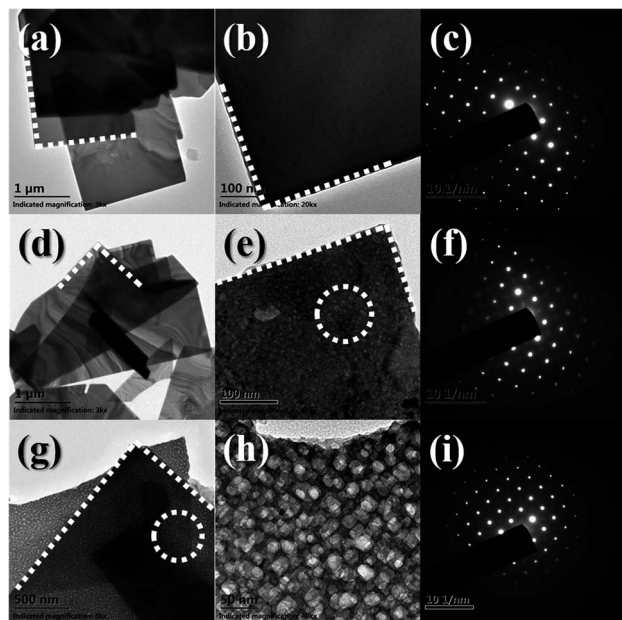Fig. 4 TEM images and electronic diffraction patterns of BOI samples: (a–c) BOI-350; (d–f) BOI-400; (g–i) BOI-450.

Fig. 6 Formation mechanism of mesoporous BOI single-crystal nanosheets.

type-IV isotherm characteristic of a mesoporous structure and a high BET area of 339 m^2 g^{-1}. The average size of the mesopores of BTO-450 was 9.2 nm, which was in agreement with the TEM observations (the inset in Fig. 5).

3.4 Formation mechanism analysis

According to the above-mentioned conclusions, the formation mechanism of these novel mesoporous BOI single-crystal nanosheets is shown in Fig. 6. At the first stage, with the reaction temperature rising, two main reactions proceed. In the first one, the surface of bulk BiI$_3$ starts to oxidize and generates BiOI and I$_2$ vapor (see chemical eqn (2)). In the second one, the internal of bulk BiI$_3$ begins to decompose in a hypoxia state and generates Bi and I$_2$ vapor (see chemical eqn (1)). Different from the surface-formed I$_2$ vapor that is easy to run off, the internally formed I$_2$ vapor is sealed by the BiOI shells and is hard to release. However, as the internal I$_2$ vapor continuously accumulates to a certain pressure, it will break and strip the surface-generated BiOI shells from the BiI$_3$ bulk layer by layer and then, the BiOI single-crystal nanosheets are obtained. At 400 °C, the generated BiOI nanosheets are oxidized by oxygen further along with the formation of I$_2$ vapor (see chemical eqn (4)). In this step, the locations occupied by I atoms in the BiOI crystal

results. The SAED patterns of BOI-350, BOI-400 and BOI-450 are displayed in Fig. 4c, f and i, respectively. It is obvious that all the three SAED patterns, taken from different crystal zone axes, exhibit similar diffraction spots array, which means these samples are all single crystals. However, unlike the smooth surface of the BOI-350 nanosheets, the surface of the BOI-400 nanosheets is more rough and full of suspected nanopore traces, as shown in Fig. 4d and the dashed box pointed in Fig. 4e. Likewise, nanopores are found on the BOI-450 nanosheets too; the difference is that the nano-pores on BOI-450 are more apparent with a mean diameter of 10 nm and run through and fill the whole nanosheets, as shown in Fig. 4g and e. This structure is very special and fascinating and for further confirmation, nitrogen adsorption/desorption measurements are obtained. As shown in Fig. 5, the BTO-450 sample has a typical
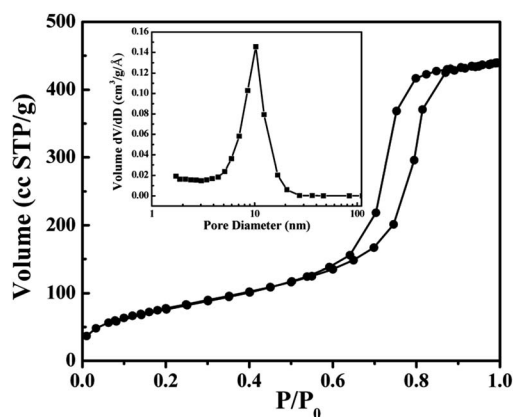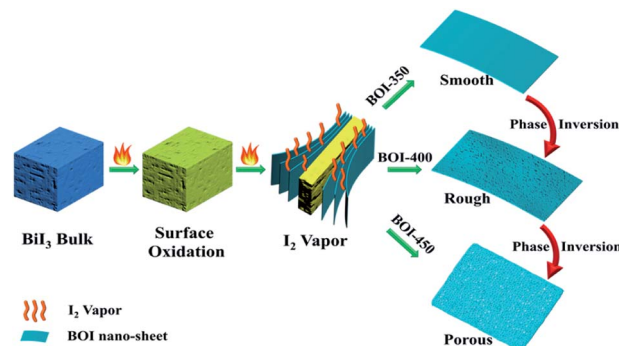

Fig. 5 Nitrogen-adsorption/desorption isotherms and pore size distributions (inset) of the BOI-450 sample.
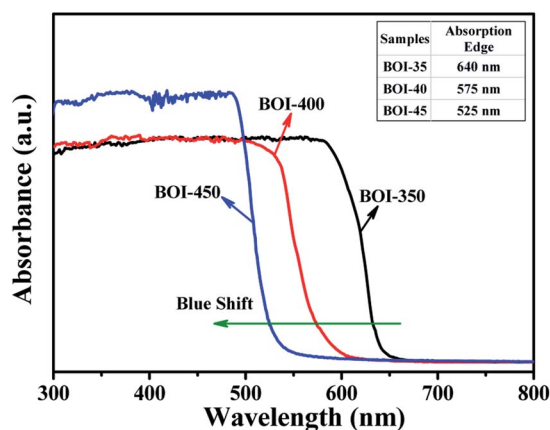

Fig. 7 UV-vis diffuse reflectance spectra of as-prepared BOI samples.

structure are vacated, leaving nanopore traces on the nanosheet surface when the I_2 vapor is released from BiOI. At 450 °C, the higher temperature accelerates the recrystallization of BiOI and the evaporation of the I_2 vapor from the outside to the inside of BiOI, leading to the formation of $Bi_4O_5I_2$ microsheets with a mass of densely distributed nano-pores running through and filling the whole nanosheets, as shown in Fig. 6.

3.5 UV-vis diffuse reflectance spectral analysis

The optical properties of the as-prepared BOI samples are investigated by UV-vis diffuse reflectance spectroscopy (DRS) (Fig. 7). All the three samples exhibit strong absorption in both visible and ultraviolet ranges. BOI-350 has the maximal absorbance wavelength and its absorption edge is 640 nm, which is in agreement with a previous result.[40] The absorption edges of BOI-400 and BOI-450 are 575 nm and 525 nm, respectively. As the arrow shows in Fig. 7, there is an apparent blue shift in the absorption edge of the samples on increasing the annealing temperature, indicating that bulk BiI_3 has been transformed thoroughly. More remarkably, the absorption strength of BOI-450 in the range of 300–500 nm is higher than that of both BOI-350 and BOI-400, implying that BOI-450 may possess better catalyst activity.[41,42]
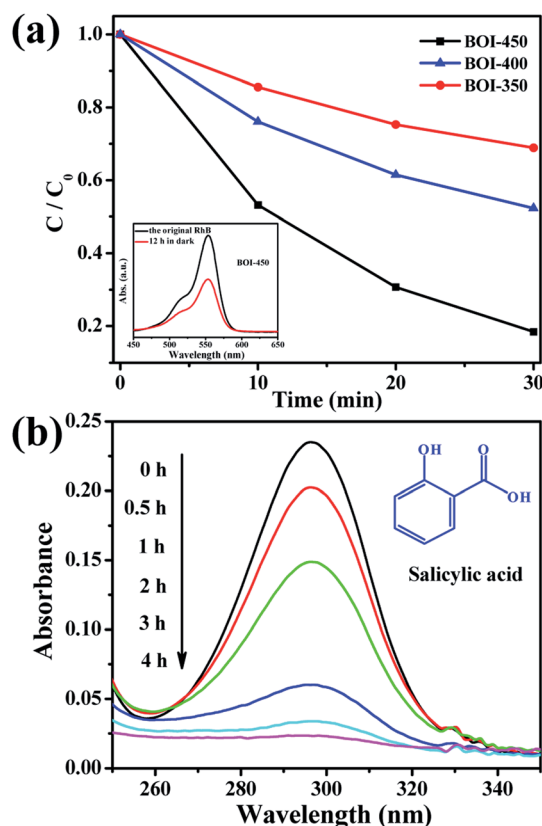

Fig. 8 Photocatalytic activities of as-prepared BOI samples. (a) Degradation curves of RhB *versus* irradiation time catalyzed by BOI samples under visible light irradiation. (b) UV-vis spectrum of salicylic acid catalyzed by mesoporous BOI-450 nanosheets.
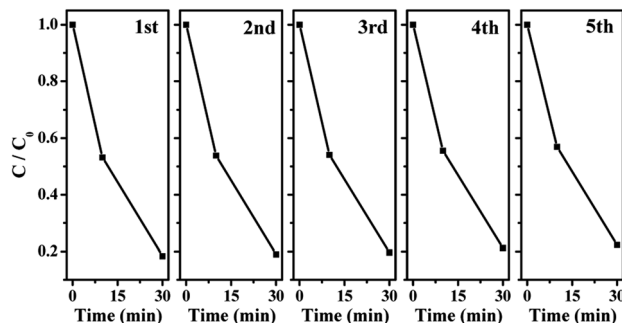

Fig. 9 The durability tests of the as-prepared BOI-450 under visible light irradiation.

3.6 Photocatalytic activity analysis

To evaluate practicability, the as-prepared BOI nanosheets are successfully employed to catalyze the removal of RhB and salicylic acid pollutants in water driven by visible light. As shown in Fig. 8a, after adsorption for 12 h in the dark, the as-prepared BOI-450 sample exhibits the best activity, and RhB can be degraded thoroughly in 30 min. Although the visible light absorption range of BOI-450 is narrower than that of both BOI-350 and BOI-400, its excellent photocatalysis ability obviously benefits from other advantages such as higher porosity (inset in Fig. 8a). For a qualified and effective catalyst, high contact capacity with the reactants is necessary. Thus, obviously, due to the porous nature of BOI-450, it has this quite remarkable ability. In order to make it more pertinent, we choose BOI-450 as the key target in the following test. For a further demonstration, another colorless pollutant salicylic acid is also used. Fig. 8b shows the corresponding UV-vis spectrum for the change in salicylic acid *versus* time. As shown in Fig. 8b, the 296 nm peak of salicylic acid can be reduced gradually in 4 h, indicating that BOI-450 indeed has excellent photocatalytic activity.

The durability of the BOI-450 sample was also tested by the degradation of RhB under visible light irradiation. As shown in Fig. 9, BOI-450 exhibits excellent stability and maintains similar photocatalytic activity after five reaction runs. Since the active component loss of the photocatalyst cannot be avoided in the recycling tests, the tiny decrease in the degradation rate of RhB is reasonable.

4. Conclusions

In summary, a novel 2D sheet-like bismuth oxyiodide single-crystal functional material with numerous mesopores was synthesized by a simple and mild heat-treatment approach. The average diameter of these pores was 9.2 nm. It was found that the formation of the as-prepared BOI nanosheets was a temperature- and reaction time-dependent process and involved crystal structure transformation. It was also demonstrated that the element I in the BOI system played an essential role in generating the 2D porous structure. Owing to this special 2D porous structure, BTO-450 displayed great activities and good stability in catalyzing RhB and salicylic acid mineralization under visible light irradiation. The 2D mesoporous

structure is beneficial to enhance the contact capacity of the catalysts with the reactants, thereby improving their reaction efficiency.

Conflicts of interest

There are no conflicts of interest to declare.

Acknowledgements

References

1 M. Chhowalla, H. Shin, G. Eda, L. Li, K. Loh and H. Zhang, *Nat. Chem.*, 2013, **5**, 263.

2 J. Coleman, M. Lotya, A. O'Neill, S. Bergin, P. King, U. Khan and K. Young, *Science*, 2011, **331**, 568.

3 S. Butler, S. Hollen, L. Cao, Y. Cui, J. Gupta, H. Gutierrez, T. Heinz, S. Hong and J. Huang, *ACS Nano*, 2013, **7**, 2898.

4 X. Quan, Y. Jia and J. Mietek, *Chem. Soc. Rev.*, 2012, **41**, 782.

5 S. Sasha, D. Dmitriy, D. Geoffrey, K. Kevin, Z. Eric, S. Eric, P. Richard, N. SonBinh and R. Rodney, *Nature*, 2006, **442**, 282.

6 H. Zhang, C. Liu, X. Qi, X. Dai, Z. Fang and S. Zhang, *Nat. Phys.*, 2009, **5**, 438.

7 M. Xu, T. Liang, M. Shi and H. Chen, *Chem. Rev.*, 2013, **113**, 3766.

8 Q. Han, B. Wang, J. Gao, Z. Cheng, Y. Zhao, Z. Zhang and L. Qu, *ACS Nano*, 2016, **10**, 2745.

9 T. Su, Q. Shao, Z. Qin, Z. Guo and Z. Wu, *ACS Catal.*, 2018, **8**, 2253.

10 M. Guan, C. Xiao, J. Zhang, S. Fan, R. An, Q. Cheng, J. Xie, M. Zhou, B. Ye and Y. Xie, *J. Am. Chem. Soc.*, 2013, **135**, 10411.

11 Y. Huo, J. Zhang, M. Miao and Y. Jin, *Appl. Catal., B*, 2012, **111–112**, 334.

12 T. Zhu, Z. Wang, S. Ding, J. Chen and X. Lou, *RSC Adv.*, 2011, **1**, 397.

13 W. Qing, K. Kourosh, K. Andras, C. Jonathan and S. Michael, *Nat. Nanotechnol.*, 2012, **7**, 699.

14 B. Francesco, C. Luigi, Y. Gui, S. Meryl, T. Valentina, F. Andrea, R. Rodney and P. Vittorio, *Science*, 2015, **347**, 41.

15 B. Alexander, *Nat. Mater.*, 2011, **10**, 569.

16 O. Painter, R. Lee, A. Scherer, A. Yariv, J. O'Brien, P. Dapkus and I. Kim, *Science*, 1999, **284**, 1819.

17 S. Sarma, *Rev. Mod. Phys.*, 2011, **83**, 407.

18 K. Novoselov, A. Mishchenko, A. Carvalho and A. Castro, *Science*, 2016, **353**, 461.

19 F. Koppens, T. Mueller, Ph. Avouris, A. Ferrari, M. Vitielloand and M. Polini, *Nat. Nanotechnol.*, 2014, **9**, 780.

20 Y. Zheng, W. Xu, H. Ya, P. Xin, Z. Zong and Q. Jie, *Carbon*, 2017, **117**, 376.

21 Z. Jian, X. You, Z. Yuan, F. Tian, W. Jie, M. Sheng and X. Li, *Carbon*, 2016, **107**, 638.

22 Y. Fan, X. Xiang, P. Hong, Y. Hua, D. Yan, L. Wen, Y. Jia, S. Qi and W. Xiang, *Appl. Catal., A*, 2015, **507**, 109.

23 S. Leng, C. Ming, R. Tie and Y. Zhong, *J. Power Sources*, 2015, **274**, 791.

24 A. Tarek, S. Osama, W. Jonas and M. Anja, *J. Mater. Chem.*, 2012, **22**, 18252.

25 A. Corma, *Chem. Rev.*, 1997, **97**, 2373.

26 M. Davis, *Nature*, 2002, **417**, 813.

27 X. Xiang, L. Lin, Y. Fan, P. Hong, F. Xiu and W. Xiang, *Mol. Catal.*, 2017, **441**, 81.

28 E. Richman, T. Brezesinski and S. Tolbert, *Nat. Mater.*, 2008, **7**, 712.

29 L. Hwan, R. Amaranath, K. Praveen, L. Manho and K. Tae, *Appl. Surf. Sci.*, 2019, **494**, 239.

30 M. Xing, F. Huan, L. Chun, L. Xiao, Z. Fan and W. Yong, *J. Mater. Sci. Technol.*, 2017, **33**, 1067.

31 Z. Yong, L. Zheng, N. Sina, A. Pulickel and L. Jun, *Small*, 2012, **8**, 966.

32 T. Alammar, O. Shekhah, J. Wohlgemuth and A. Mudring, *J. Mater. Chem.*, 2012, **22**, 18252.

33 L. Ye, L. Tian, T. Peng and L. Zan, *J. Mater. Chem.*, 2011, **21**, 12479.

34 S. Sun, W. Wang, L. Zhang, L. Zhou, W. Yin and M. Shang, *Environ. Sci. Technol.*, 2009, **43**, 2005.

35 W. Lee, C. Lu, C. Chuang, Y. Chen, J. Fu, C. Siao and C. Chen, *RSC Adv.*, 2015, **5**, 23450.

36 R. Yin, Y. Li, K. Zhong, H. Yao, Y. Zhang and K. Lai, *RSC Adv.*, 2019, **9**, 4539.

37 J. Hou, J. Tang, K. Feng, F. Idrees, M. Tahir, X. Sun and X. Wang, *Mater. Lett.*, 2019, **252**, 106.

38 X. Xiao, C. Xing, G. He, X. Zuo, J. Nan and L. Wang, *Appl. Catal., B*, 2014, **148–149**, 154.

39 C. Chun, Y. Huan, M. Wei, C. Yan, W. Li, Y. Li and Q. Hong, *Appl. Catal., B*, 2019, **254**, 647.

40 J. Hu, S. Weng, Z. Zheng, Z. Pei, M. Huang and P. Liu, *J. Hazard. Mater.*, 2014, **264**, 293.

41 C. Yu, G. Li, S. Kumar, K. Yang and R. Jin, *Adv. Mater.*, 2014, **26**, 892.

42 T. Jamil, E. Mansor and M. El-Liethy, *J. Environ. Chem. Eng.*, 2015, **3**, 2463.